

CHALMERS



Finding the Jeffrey Orbits

Master's Thesis in Complex Adaptive Systems

Staffan Ankardal

Department of Applied Physics
CHALMERS UNIVERSITY OF TECHNOLOGY
Gothenburg, Sweden 2013
Master's Thesis 2013:1

Abstract

The Jeffery orbits define the motion of axissymmetrical particles in shear flow and is thus important in the study of suspensions of particles. In this thesis I attempt to verify the equations of motion experimentally using glass particles in a reversible flow in a microfluidic PDMS channel and an optical tweezer. An automatic tracking of the particles was developed and a number of improvements were made compared to previous experiments such as by Einarsson et al[1]. We study the effects of asymmetry on the particles and the transition from periodic to quasi-periodic orbits for different initial conditions of particles and for different degrees of asymmetry. One good match with theoretical results is found for some measurements, but there are some unexplained behaviours when the flow is reversed.

Acknowledgements

I hereby wish to thank my Supervisors Bernhard Mehlig and Dag Hanstorp for helping me through this journey. I want to thank girlfriend Callie Gibbons for supporting me through the work on this thesis and Alexander Laas for being a tireless and understanding co-worker. I want to thank all the contributors to the wealth of open source software which I have used to create everything from most of the software to more of the figures and of course this very report.

Staffan Ankardal, Göteborg Sweden INSERT PROPER DATE 3/11/13

Contents

1	Introduction	1
1.1	Introduction	1
1.1.1	Background	1
2	Theory	4
2.1	Fluid Dynamics	4
2.1.1	Reynold's Number	4
2.1.2	Stokes Drag and Stokes's law	5
2.2	Euler Angles and our Coordinate System	6
2.2.1	Triaxial particles	7
2.3	Jeffery Orbits	8
2.3.1	Winding Number	11
3	Method	14
I	Improvements of Experimental Setup	15
3.1	Experimental Setup	16
3.1.1	List of equipment	19

3.2 Improvements	19
3.2.1 Particles and Channel	20
3.2.2 Automated Tracking	22
3.2.3 Acquiring the image	23
3.2.4 Reducing noise	23
3.2.5 Contour detection and selection	24
3.2.6 Adjusting the Camera velocity	24
3.2.7 Time Considerations	25
II Data Analysis and Results	26
4 Data Analysis	27
4.0.8 Particle identification	27
4.0.9 Estimation of orientation	28
4.0.10 Width compensation	29
4.1 brushing	30
4.2 Winding number estimation	31
4.3 Matching to theoretical orbit	33
5 Results	34
5.1 Particle A	35
5.1.1 Measurement 1	35
5.1.2 Measurement 2	38
5.1.3 Measurement 3	38
5.1.4 Measurement 4	39
5.1.5 Measurement 5	39
5.2 Particle B	41
5.2.1 Measurement 1	43
5.2.2 Run 1	43

5.2.3	Measurement 2	45
5.2.4	Measurement 3	46
5.2.5	Measurement 4	47
6	Discussion	48
6.1	Sinking	48
6.2	Reversals	49
6.2.1	Velocity behaviour	49
6.3	Winding number matching	50
6.4	Unexplained behaviours	51
7	Conclusion	52
A	Raw data	53

1

Introduction

1.1 Introduction

My goal in this thesis is to study and better understand the dynamics of ellipsoidal particles in shear flow. It is a continuation of two previous masters theses [2, 3]. This is done by analysing micrometer length glass particles in a shear flow and comparing this to theoretical models. In the first part of the thesis I will write about the improvements that were made to the experimental setup including an automated tracking. In the second part the measurements and the analysis of them are discussed. Before discussing either of these processes more in depth some background and theory is needed.

1.1.1 Background

Understanding the dynamics of particles in flow might appear somewhat esoteric but there is actually a number of topics where it is important. In fluid dynamics non-newtonian fluids are often high concentrations of particles suspended in liquid, such ketchup or blood, and understanding their behaviour might need an improved understanding of how each individual particle will behave. In medical applications understanding the dynamics of ellipsoidal particles like bacteria can be rele-

1.1. INTRODUCTION

vant to a detailed understanding of their interactions with cells and other bodies as discussed by Tolga *et al*[4].

The study of particle dynamics in flow began with Einstein's in 1905 [5] in which he showed how much the suspended spherical particle would increase the viscosity of a fluid. Jeffery in his 1922 paper [6] extended these results to ellipsoidal axis-symmetrical ellipsoidal particles and derived equations for the orientational dynamics of the particles, in other words how the particles would rotate as a function of time. For systems where inertial effects could be discarded the motion was found to be periodic and depending only on the initial condition of the particle.

Investigation of triaxial particles was started by Gierszewski & Chaffey[7] and was continued by Hinch & Leal[8] and more recently by Yarin *et al*[9]. The dynamics found for axis-symmetric particles by Jeffrey were periodic, but it was shown by Hinch & Leal that some orbits would be doubly periodic, in other words following two separate independent periods. This behaviour will here be referred to as quasi-periodic.

Yarin was able to use numerical simulations to generate a surface of section [10] for some asymmetric relations between the two minor axes showing that not only was there double periodic or quasi periodic orbits but for sufficiently large asymmetries there would be chaotic orbits. Several other surfaces of section were produced by Johansson [2] using the same method as Yarin with higher resolution thanks to improvements in computing power. It was shown that even small asymmetries on the order of 1% will lead to quasi-periodic motion for some initial conditions.

Attempts to experimentally verify these theoretical results were first performed by Goldsmith and Mason in 1962[11] who used flow in a glass pipe to observe the rotation rate for several different particle shapes. He was able to confirm that the rotation rate matched well with that predicted from Jeffery orbits but he did not study the actual orbits. Since then most experimental research, such as by Harlen and Koch[12] has been focused on how diluted suspensions of particles effect the properties of a liquid. Only tangential efforts such as by Tolga[4] were concerned with the Jeffery orbits. A good summary of both theoretical and experimental results was written by Petrie[13] in 1999.

The first dedicated experiments to measure the actual Jeffery orbits in angular components and

1.1. INTRODUCTION

verify the orientational dynamics was done by Einarsson *et al* [1] in 2011. Although there was some promising results, the vast majority of particles were asymmetric to the point of chaotic or highly quasi-periodic. Moreover the width and length of particles both varied greatly and could not be measured accurately. This meant that although the orbits could be qualitatively shown to be similar to some Jeffery orbits no particular particle could be shown to exhibit both quasi periodic and periodic motion, and there was no particle that could be well matched to a particular orbit. There was also few particles that showed a perfectly identical reversal through the entire length of the channel when the flow was reversed.

The goal of this thesis is to experimentally verify the results of Yarin and Hinch, Leal[8, 9] and show that the same particle will show different types of motion for different initial conditions and furthermore that different particles will also show different motion for the same initial conditions based on the asymmetry. This is done by observing the orientation of a micrometer length particle in a creeping shear flow. The flow is shown to be a creeping by demonstrating that the particle dynamics revert as the flow is reverted. The results for different initial conditions will then be compared to theoretical predictions.

2

Theory

In order to better understand the results and discussions in this thesis some rather basic knowledge in fluid dynamics, image analysis and other fields is needed.

The focus of this thesis is experimental, so this chapter will not be entirely thorough. A more inquisitive reader is recommended to read Einarssons thesis [3] which goes into greater detail on most of the topics covered in this section.

2.1 Fluid Dynamics

In order to understand the motivations, limitations and behaviour of the experiment we need to know about a few key concepts in fluid dynamics.

2.1.1 Reynold's Number

The Reynolds number (Re) is a dimensionless number describing the ratio of inertial forces to viscous forces in a flow. For flow in a pipe it is defined by Pedley [14] as

$$Re = \frac{UL\rho}{\mu} \quad (2.1)$$

2.1. FLUID DYNAMICS

where U is the characteristic velocity of the flow, L is the characteristic length, ρ is the density and μ is the dynamic viscosity. This is used to estimate the 'regime' of the flow, of which there are two primary types.

1. Laminar flow, where viscous forces dominate over inertial forces
2. Turbulent regime where inertial forces dominate.

The Reynolds number is a ratio between the inertial forces and viscous forces, so we get more turbulent flow for larger Reynolds numbers. A simple visual characterization of the flow types can be seen in figure 2.1. $Re \ll 1$ is referred to as *Stokes flow* where we can ignore inertial forces completely. This means that not only is the flow completely guaranteed to be laminar, but it is time reversible. Reversing the direction of a Stokes flow and any dynamics of the flow and particles in the flow will revert perfectly as well [15].

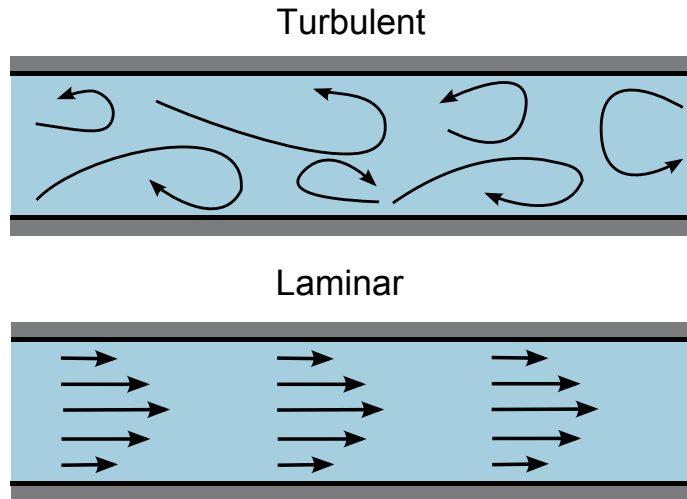


Figure 2.1: This shows the principal difference between laminar and turbulent flow.

2.1.2 Stokes Drag and Stokes's law

The drag force F_D exerted by a fluid on a spherical particle for $Re \ll 1$ is found using the so called Stokes's law [16]

$$F_D = 6\pi\mu Rv, \quad (2.2)$$

where v is the velocity of the sphere relative to the fluid, μ is the dynamic viscosity and R is the radius of the sphere. The terminal velocity of a sphere sinking in a liquid is found by equating the gravitational force F_G acting on the sphere with the drag force. F_G is

$$F_G = \Delta\rho g \cdot \frac{4\pi R^3}{3}, \quad (2.3)$$

where $\Delta\rho$ is the difference in density and g is the specific gravity. We find that the terminal velocity of a sinking (or floating) sphere is

$$v_s = \frac{2}{9} \frac{\Delta\rho}{\mu} g R^2. \quad (2.4)$$

This is referred to as Stoke's Law.

2.2 Euler Angles and our Coordinate System

When describing rotating particles it is common to use the so called Euler angles. A formal definition is given by Weber *et al* [17] but for the purposes of this thesis we will describe it as a transformation from our stationary coordinate system $\{x,y,z\}$ to the coordinate system attached to our particle $\{x',y',z'\}$. This transformation is performed in three steps by using the intermediate axis T.

- Rotate the x-y plane ϕ about the z-axis.
- Denote the shifted x axis T and rotate the z-y' plane θ around this axis
- Rotate ψ around the z' axis to obtain the final coordinate system

This is illustrated in figure 2.2a where each prim marks one more step of rotation to the coordinate system. Figure 2.2b shows the Euler angle rotations for a triaxial particle shown from a point

of view similar to the of the experiment where the X-Z plane is the primary plane. This means we can describe the orientation of a particle using $\mathbf{E} = (\phi, \theta, \psi)$.

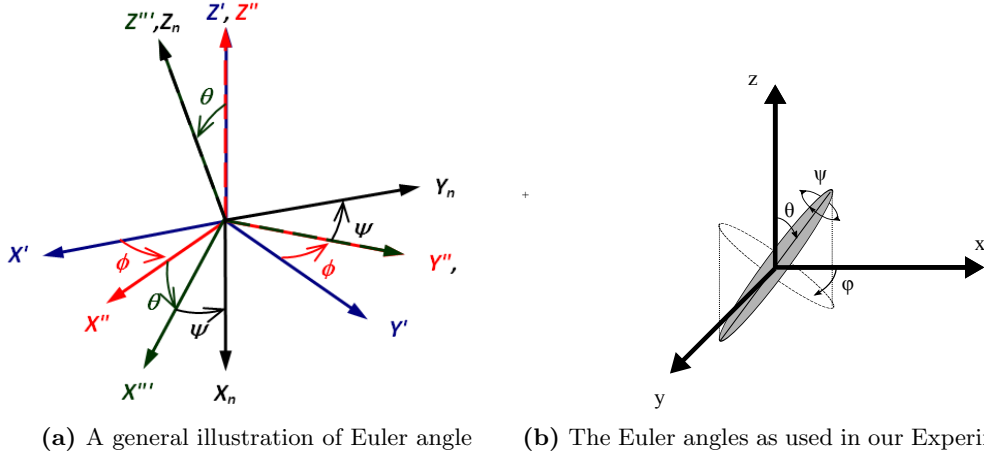


Figure 2.2: Figure (a) shows the Euler angles illustrated using a series of coordinate rotations. Figure (b) show the Euler angles illustrated using an ellipsoid. This alternate visualization shows the angles with a point of view similar to that of the camera in the experiment. ψ has an impact on the particle dynamics but we can not observe it as the particle is nearly axis-symmetric.

2.2.1 Triaxial particles

Triaxial particles have, as the name suggests, three axis which are all distinct, compared to a sphere which has only one and an ellipse that has two. I will in this thesis refer to the lengths of these axes as a_x, a_y, a_z corresponding to their lengths along those axes for $\mathbf{E} = (0,0,0)$.

It is, when discussing triaxial particles that are close to being axissymmetric or ellipsoids of the form $a_x \gg a_y \approx a_z$, convenient to introduce the particle asymmetry ϵ defined as

$$\epsilon = \frac{a_y}{a_z} - 1, \quad (2.5)$$

and the aspect ratio λ given by

$$\lambda = \frac{a_x}{a_y}. \quad (2.6)$$

2.3 Jeffery Orbits

The Jeffery Orbits describe the motion of an ellipsoidal particle in stokes shear flow as a function of time. The initial orbits found by Jeffery were for axis-symmetrical ellipsoidal particles, but was generalized by Yarin *et al* [9] to triaxial particles. The Jeffery orbits are sometimes referred to the symmetric orbits but I will in this thesis refer to the generalized orbits as the Jeffrey Orbits. The generalized equations of motion found by Yarin *et al* was

$$\frac{d\theta}{dt} = (g_2 \sin \psi + g_3 \cos \psi) \sin \theta, \quad (2.7a)$$

$$\frac{d\phi}{dt} = \frac{1}{2} + g_3 \sin \psi - g_2 \cos \psi, \quad (2.7b)$$

$$\frac{d\psi}{dt} = g_1 + (g_2 \cos \psi - g_3 \sin \psi) \cos \theta \quad (2.7c)$$

$$(2.7d)$$

where the functions g_i are defined as

$$g_1 = \frac{a_y^2 - a_z^2}{2(a_y^2 + a_z^2)} \left(-\frac{1}{2}(\cos^2 \theta + 1) \sin 2\phi \sin 2\psi + \cos \theta \cos 2\phi \cos 2\psi \right), \quad (2.8a)$$

$$g_2 = \frac{a_z^2 - a_x^2}{2(a_x^2 + a_z^2)} \left(-\cos \theta \sin 2\phi \sin \psi + \cos 2\phi \cos \psi \right), \quad (2.8b)$$

$$g_3 = \frac{a_x^2 - a_y^2}{2(a_x^2 + a_y^2)} \left(\cos \theta \sin 2\phi \cos \psi + \cos 2\phi \sin \psi \right). \quad (2.8c)$$

The definition of the Euler angles (ϕ, θ, ψ) is seen in figure figure 2.2a. Solutions to the equations of motions can be found with numerical methods as shown by [9] but one has to be careful to convert to the right coordinates. The time evolution of θ and ψ for different initial conditions can be plotted in a Poincaré map, also known as a Surface of Section (S.O.S.) [18] for $\phi = 0$. The points for every initial condition is bound to a certain region of such a map called the orbit. A few such maps can be seen in figure 2.4

2.3. JEFFERY ORBITS

For a particle with an $\epsilon \in [0.01 - 0.05]$ there are essentially three classes of orbits.

1. **Periodic:** For larger $|\theta|$ in which there is little variation and the particle is largely periodic with fluctuations too small to measure.
2. **Quasi-periodic bent:** For intermediate $|\theta|$ the amplitude of $\cos(\theta)$ changes noticeably but does not change sign.
3. **Quasi-periodic circular:** For small $|\theta|$ the amplitude of $\cos(\theta)$ will change noticeably and change in sign from positive to negative.

For larger asymmetries $\epsilon > 0.05$] there will also be chaotic orbits that will appear as areas with dots. Such orbits can be seen in figure 2.4d.

These three different types of orbits are illustrated in figure 2.3 both on the S.O.S. as well as the components of \mathbf{n} . We can see that while n_x and n_y are periodic but with different amplitudes the behaviour for n_z is significantly different. For the large n_z orbit shown in green there is very little variation over time, only a slight modulation. For the bent quasi periodic orbit in red there is a far more significant modulation with a fixed period. For the circular quasi periodic orbit in blue n_z changes sign, again with a fixed period.

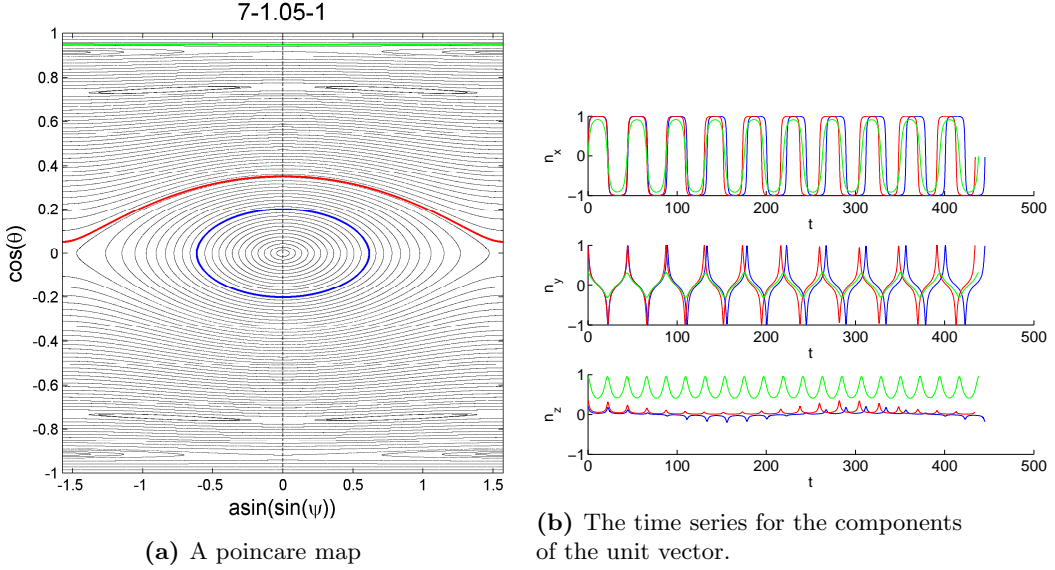


Figure 2.3: A poincare map and three orbits for the Jeffery orbits of a particle with $\lambda = 7$ and $\epsilon = 0.05$. The three orbits highlight the three different kinds of orbit, the quasi periodic circular orbit in blue, the quasi-periodic bent orbit in red and the periodic in green. We see that while n_x and n_y look qualitatively similar but differ in amplitude for the different orbits n_z shows three different types of behaviour

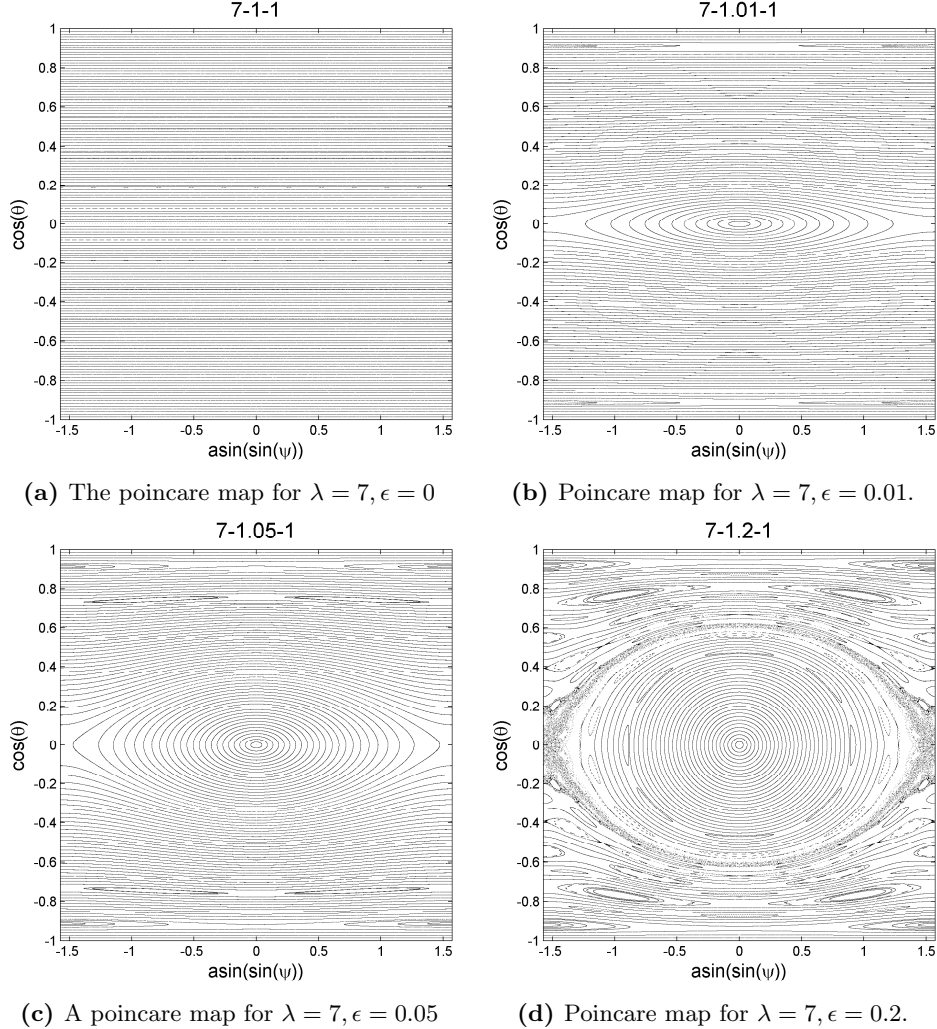


Figure 2.4: Four Poincare maps for different ϵ . Already at $\epsilon = 0.01$ there are noticeably quasi-periodic orbits around the centre at $\cos(\theta) \approx \psi \approx 0$ but it is also a significantly larger region for $\epsilon = 0.05$. For $\epsilon = 0.2$ we can see chaotic orbits surrounding the circular orbits in the centre that appear as a 'sea' of dots.

2.3.1 Winding Number

The quasi-periodic orbits are also referred to as double-periodic [9]. This is referring to the fact that the variations that are seen in figure 2.3b are periodic as well. The ratio between the two periods is referred to as the winding number ω , or simply

$$\omega = \frac{\theta_1}{\theta_2}. \quad (2.9)$$

This is illustrated in figure 2.5.

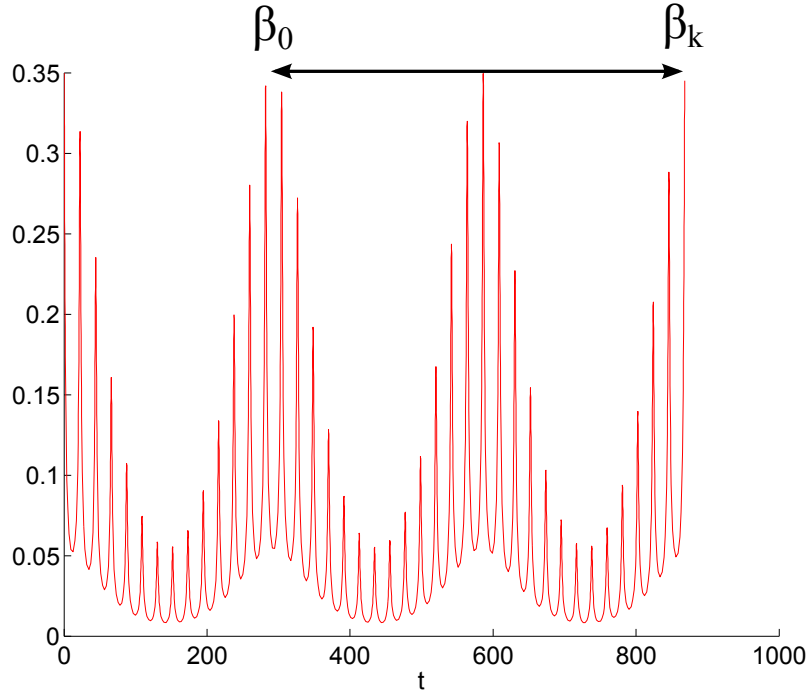


Figure 2.5: The n_z plot bent quasi periodic orbit from figure 2.3b highlighting the short period θ_2 which is simply the period of ϕ and the longer period θ_1 . The winding number is defined as the ratio between the longer and shorter periods.

This can also be thought of as the number of steps travelled on the poincare map before coming back to where it started, divided by the number of laps it takes. This number is the same for any point along a given orbit on the poincare map but varies greatly for different orbits as well as for different asymmetries. The winding numbers for orbits along $\psi = 0$ for $\epsilon = \{0.01, 0.05, 0.10\}$ can be seen in figure 2.6. This shows us that if we can measure the winding number we should be able to approximate the asymmetry of the particle fairly well, especially if we can see the gap between a quasi periodic bent orbit and a circular orbit.

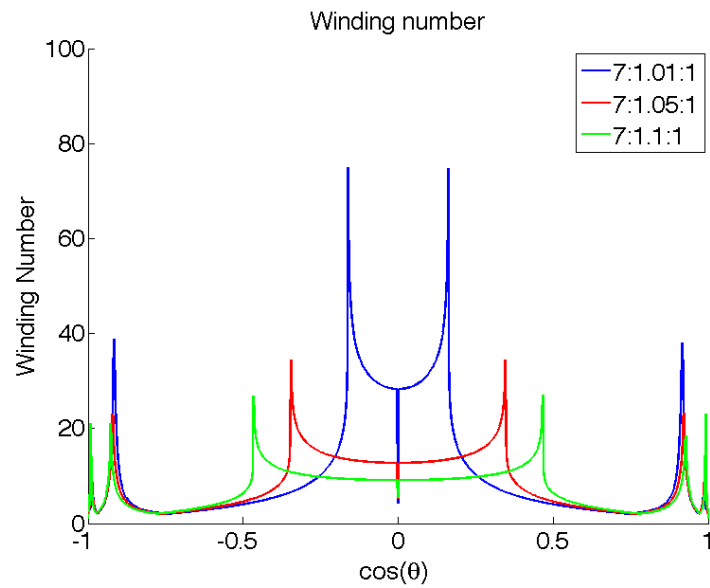


Figure 2.6: The winding number as a function of $\cos(\theta)$ for three different asymmetries. The sharp edge that occurs centered around zero is where the circular orbits change into bent orbits. We see that a lower asymmetry leads to a sharper difference between the circular and the bent orbits.

3

Method

Part I

Improvements of Experimental Setup

3.1. EXPERIMENTAL SETUP

3.1 Experimental Setup

The motion of particles in a liquid was studied by pumping a liquid through a microfluidic channel. The channel is placed on a moveable stage on top of a microscope. A particle can be tracked by moving the stage to match the velocity of the particle in the channel and thus keep the particle stationary in the field of view of the microscope. Connected to the microscope is a CCD camera recording the images and these movies are saved on a computer. As the particle gets within 1 cm of the inlets on the channel the flow is reversed. We will refer to the data of a particle along one such length of the channel a **stretch** and a series of stretches for a single particle a **measurement**. A sketch of this setup can be seen in figure 3.3a and a photograph of the actual setup in figure 3.2.

Between measurements, optical tweezers (for details on how it works see [19]) constructed by A. Laas [20] was used to change the initial condition of the particle.

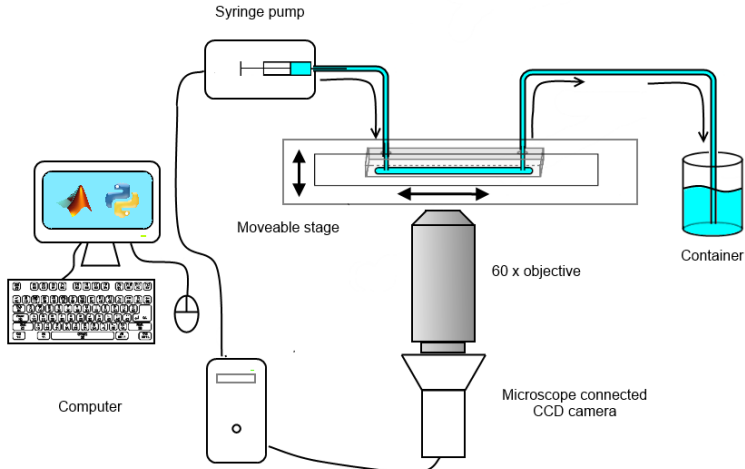


Figure 3.1: Sketch of the set up

3.1. EXPERIMENTAL SETUP

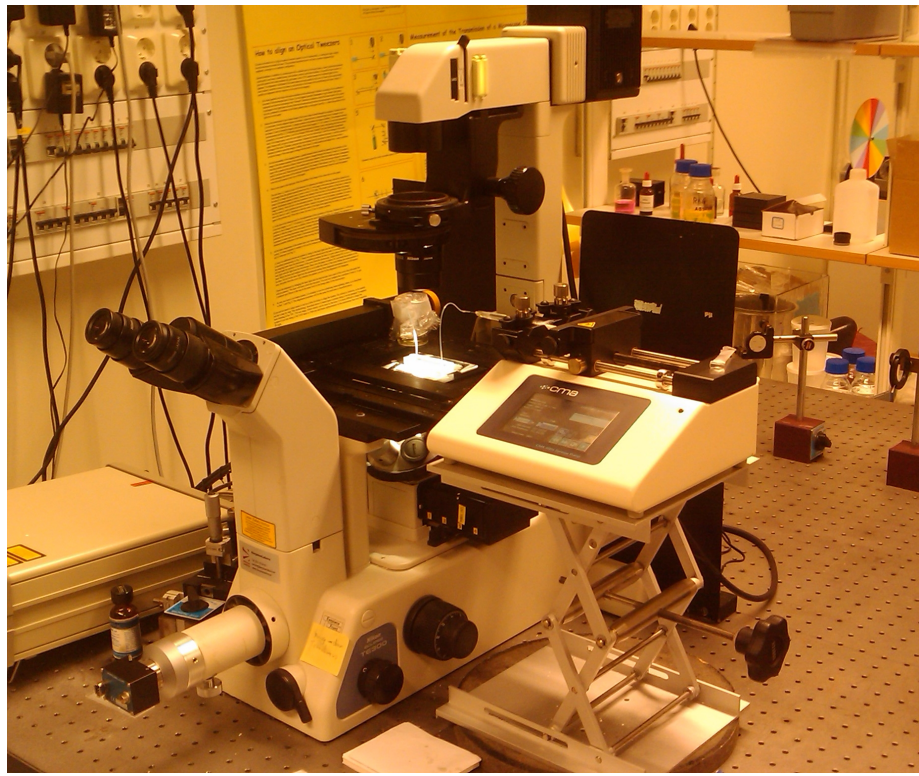


Figure 3.2: Overview of the set up. The microscope to the left and the syringe pump to the right. The CCD camera is mounted on the left side of the microscope and cannot be seen in this picture.

The microfluidic channel is 40 mm long, 2.5 mm wide and ca unit[150] μm deep. The channel is made from Polydimethylsiloxane (PDMS) and plasma bonded to a microscope slide, a more detailed description of the process can be found from the Caroline Workshop [21]. This material and procedure is chosen so that a particle that gets filled with dirt or breaks can cheaply and easily be replaced and because it's non reactive and highly transparent. A sketch of the channel can be seen in figure 3.3a and a photograph of an actual channel can be seen in figure 3.3b.

3.1. EXPERIMENTAL SETUP

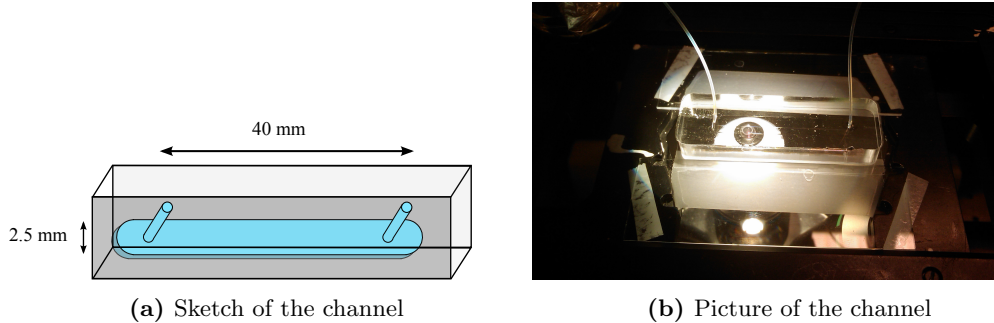


Figure 3.3: A sketch of the channel as well as a picture of the channel as it is set up during a measurement. The channel is only $150\ \mu\text{m}$ deep, but the PDMS surrounding it is around 15 mm to try and prevent the channel from expanding and contracting too much.

To find the maximum flow speed of the channel we need to know the flow profile and using the software used in Johansson [2] we get the flow profile that can be seen in figure 3.4. Integrating the flow profile over the entire surface will give us an effective flow area. To find the maximum flow speed we can simply divide the flow rate by the effective flow radius.

DO THIS SOME TIME SOON OKAY?

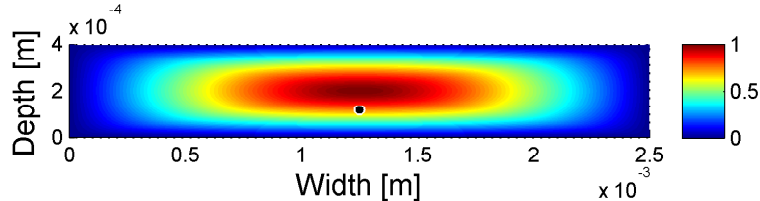


Figure 3.4: The theoretical estimation of the flow profile. Image used with permission from Johansson [2]

To confirm that the flow is a creeping flow we can calculate the maximum Reynolds number using eq 2.1 and our maximum flow speed.

$$\text{Re} = \frac{UL\rho}{\mu} \leq \frac{6.66 \cdot 10^{-3} \cdot 2.5 \cdot 10^{-3} \cdot 2.5}{24 \cdot 10^{-3}} \approx 1.6 \cdot 10^{-3} \ll 1 \quad (3.1)$$

This should satisfy the conditions of the Jeffrey equations. To track the particles the channel is put in a moveable stage on a confocal microscope. The entire setup can be seen in figure

3.1.1 List of equipment

The equipment used during the experiment is as follows

- Leica DFC350 FX digital camera
- Nikon Eclipse TE 300 microscope
- Nikon 60x water immersion objective
- Märzhäuser Wetzlar 'LStep-eco' step engine
- CMA 4004 syringe pump
- Laser

3.2 Improvements

As previously mentioned this thesis is a continuation of work done by Mehlig *et al*, Einarsson *et al* and Mishra *et al* [1, 2, 22]. Their results were promising but there were a number of key limitations and problem that need to be solved in order to improve the results. They can be summarized as:

1. The particles

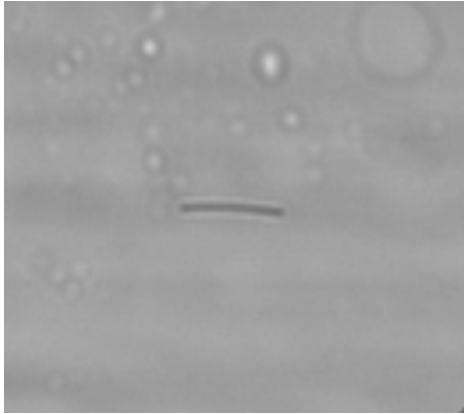
- Very few particles used in previous experiments were symmetric. Most were visibly bent or uneven, see figure 3.5
- The average aspect ratio of the particles was very high which meant there were very few flips along a stretch.
- The width of the particles could not be measured, is not uniform and very small which makes estimates of the aspect ratio hard.
- The particles could not be trapped with an optical tweezers due to low transmittance.

2. The PDMS in the channel was very jagged which caused a great deal of noise unless the focus was in a very narrow band.

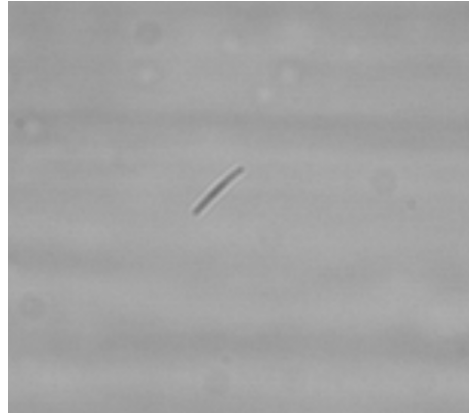
3.2. IMPROVEMENTS

3. Manual tracking of particles was time consuming and mentally draining.
4. Bubbles are difficult to avoid when setting up the experiment

3.2.1 Particles and Channel



(a) Particle 13 from July 2012



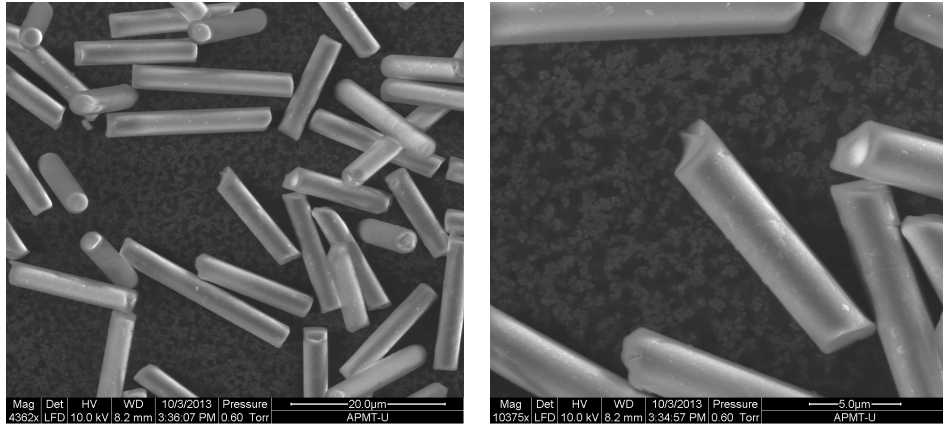
(b) Particle 22 from July 2012

Figure 3.5: Two fairly typical particles from the previous setup. Note that these are still selected from the total pool of particles for being relatively symmetric and yet are noticeably bent.

The particles were replaced with glass particles from Nippon Glass, Japan [23]. The new particles are made from LCD spacing rods that are broken into pieces. This means that they are essentially broken cylinders with very homogeneous widths but quite disparate lengths. Two different batches of particles have been used, one with $3\mu m$ diameter and one batch with $5\mu m$ diameter. All the particles presented in the results section are from the $3\mu m$ batch. The symmetry of the particles was investigated by taking images with an ESEM (Environmental Scanning Electron Microscope) with the help from Stefan Gustafsson, shown in figure 3.6. We see that the particles are uniformly smooth along the sides but have varyingly jagged edges causing different degrees of asymmetry.

In particular figure 3.7b shows a top down view of a particle clearly showing a very circular shape with no discernible asymmetry whereas figure 3.6 show the jagged edge of several particles.

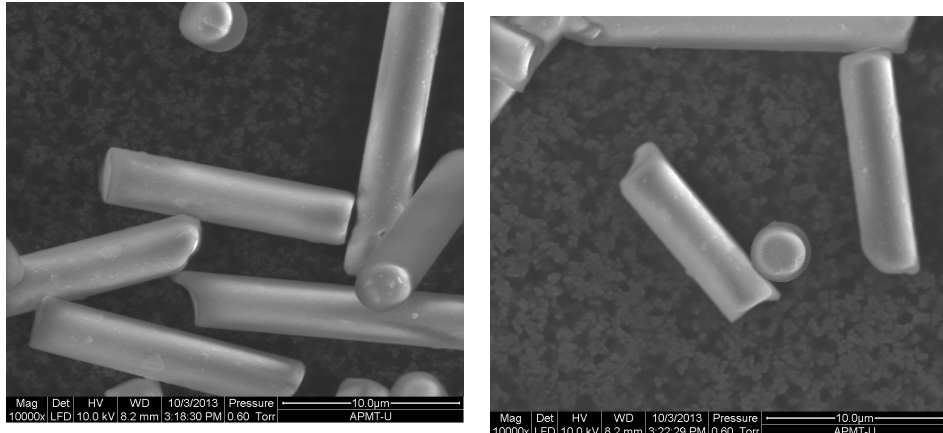
3.2. IMPROVEMENTS



(a) Shows a detailed view of a number of particles.

(b) Shows in detail the jagged edge of a particle.

Figure 3.6: Pictures of the glass particles that were used. Their width is highly uniform and there is a noticeable variance in asymmetry. Some particles show very clearly jagged edges while others appear very smooth. This suggests that they should have quite different ϵ and then exhibit quite different behaviour.



(a) What appears to be a highly symmetric particle.

(b) A top down view of a particle.

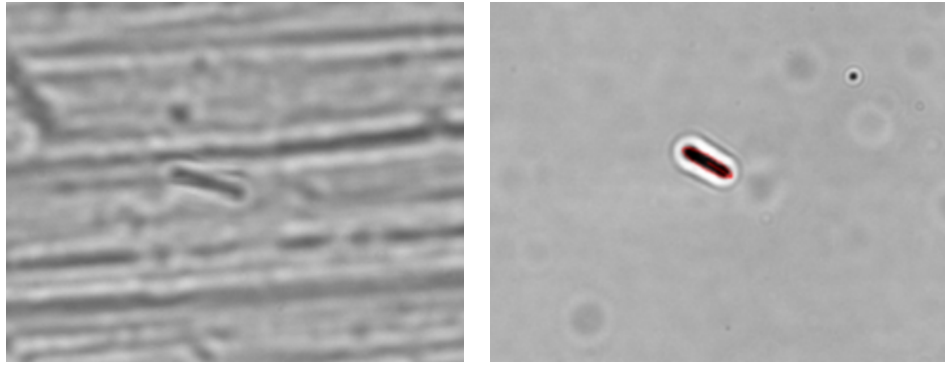
Figure 3.7: Pictures highlighting the roundness of the particles as well as the apparent symmetry of some particles. It should be noted that although there are no apparent rough edges there was no way to rotate a sample so there might very well be asymmetries on the side of the particle that we cannot see.

While these particles seemingly satisfy the symmetry conditions they are made of glass with a density of approximately 2.57 g/cm^3 at 20°C . This is significantly higher than that of water with

3.2. IMPROVEMENTS

a density of 1 g/cm^3 at 20 C° and glycerol with a density of 1.5 g/cm^3 . Thus to correct for the density and limit sinking or floating the water soluble Sodium metatungstate which at 20 C° has maximum density of 2.94 g/cm^3 is added to the liquid. To increase the viscosity of the liquid around 8% glycerol is added and the liquid was measured using a MCR 302 rheometer to have a dynamic viscosity of $24 \cdot 10^{-3}\text{ Pa s}$.

A problem in finding and tracking a particle was that the surface of the PDMS was very uneven and sharp ridges along the length of the channel appear like in figure 3.8a unless the focus was in a relatively narrow depth of the channel.



(a) An unusual severe case of the PDMS edges creating noise. (b) After being polished there is no trace of such ridges.

Figure 3.8: Pictures highlighting the roundness of the particles as well as the apparent symmetry of some particles. It should be noted that although there are no apparent rough edges there was no way to rotate a sample so there might very well be asymmetries on the side of the particle that we cannot see.

This was fixed by polishing the copper mold in which the PDMS channels are formed with a silicate abbrasive (Autosol) and emery cloth. This reduces all visible scratches from the mold and thus from the PDMS and the result can be seen in figure 3.8b.

3.2.2 Automated Tracking

One of the most time consuming aspects as well as mentally draining is manually tracking a particle. Depending on the flow rate and the number of stretches and runs desired for a particle it can take several hours. Thus one of the primary targets for improvement as discussed by Johansson [2] was

to make the camera tracking automatic. This would enable faster measurements as well as more measurements since it would reduce fatigue.

Such a tracking was implemented using Python and the external packages `OPENCV`, `NumPy`, `SciPy`, `ImageMagick` and `ctypes`. The goal of the tracking is relatively similar to the tracking described in 4.0.8 and more in detail in Johansson [2]. There are however a few very important differences that produce unique problems outlined below.

3.2.3 Acquiring the image

The first step in this is to acquire the image from the microscope in order to identify (and track) the particle. However the Leica DFC350 FX camera only works with the proprietary Leica software which means there is no easy way to get this image straight from the camera in real time. This meant we were forced to use the `ImageGrabber` package in Python and then isolate the camera image from the screen. This quite easy to do but takes ca 50 ms per frame which would be unnecessary for an open source camera software.

3.2.4 Reducing noise

The first step to reducing noise is to reduce the static noise from the movie caused by dirt, scratches and other defects in the microscope and on the camera lens, as shown in figure 4.1a. As the noise is static and everything else changes this is a simple matter of computing an average frame \bar{F} . We have N frames F_i and then

$$\bar{F} = \frac{\sum_{i=1}^N F_i}{N}. \quad (3.2)$$

An example of such an average frame can be seen in figure 4.1b. This is then removed from each of the camera frames \bar{F}_i and the result can be seen in figure 4.1c. After this we apply a smoothing function and Canny edge detection [24] and then use the resulting edge image.

3.2.5 Contour detection and selection

Once an edge image has been generated, we use the OpenCV command, `Contours` which returns a list of every contiguous group of edge pixels. If we have chosen the threshold values to the edge detection correctly, this should include the particle or a good approximation of it. In order to find the correct contour a few techniques are used.

First, contours whose total size is less than some minimum value, n_{min} or larger than some maximum value n_{max} are ignored. Then the position P_i of each contour $C_i = p_1, p_2 \dots p_n$ is calculated as the average pixel position

$$P_i = \sum_j^n p_j / n$$

This position is compared to the expected position of the particle , which the very first frame is the middle position and thereafter is assumed to have constant speed.

Finally a 'thinness value' is calculated using

$$w_{thin} \left(\frac{n}{d_{max}^2} \right)^2, \quad (3.3)$$

where w_{thin} is a weighting constant, n is the number of pixels in the contour and d_{max} is the longest distance between two pixels in the contour.

3.2.6 Adjusting the Camera velocity

Once detected twice the particle will have some velocity relative to the camera v_{rel} and a position \mathbb{P} . If the velocity is larger than some threshold v_{thresh} or the position is outside a center square in the image, $\mathbb{P} \notin \mathbf{B}$ we want to adjust the velocity of the step engine.

We then simply do a straight correction but with a damping factor ζ to prevent a feedback loop. So our resulting velocity change V_c is

$$V_c = v_{rel} \cdot \zeta. \quad (3.4)$$

3.2.7 Time Considerations

A higher frame rate will allow for greater predictive power and increase stability as the error between frames is reduced. Reducing computational time of each task is important for optimizing the tracking which also means knowing what tasks are the most demanding. A list of the different tasks and their average execution times can be seen in table 3.1

NOTE CURRENTLY NOT PUT IN ACTUAL DATA ONLY APPROXIMATE

Task	Average time	Std deviation
Capture screen	1000	200
Find edges	200	20
Change velocity	400	50

Table 3.1

We see that the FPS is limited primarily by three routines: The screen capture routine, the change velocity routine and finally the save position routine. The first and last are unavoidable and must be done every frame by definition if we are interested in knowing the particles position as well as possible. This means we simply want to use the velocity correction as little as possible. Since the time constraint is in the communication with the step engine, there is not any optimization to be done here, at least not within the scope of this thesis.

Part II

Data Analysis and Results

4

Data Analysis

Once a movie had been recorded we want to estimate the dynamics of the particle. This is done in several steps.

4.0.8 Particle identification

The first step of the data analysis is to reduce the static noise from the movie caused by dirt, scratches and other defects in the microscope and on the camera lens as can be seen in figure 4.1a. As the noise is static and everything else changes this is a simple matter of computing an average frame as in equation 3.2

An example of such an average frame can be seen in figure 4.1b. The Average frame is removed from the camera frame and the result can be seen in figure 4.1c. After this we apply a smoothing function and Canny edge detection [24] and fill the resulting edge. The resulting pixels are then fit to an ellipse as described in [2, 25]. The filled contour and the fit ellipse can be seen in figure 4.1d.

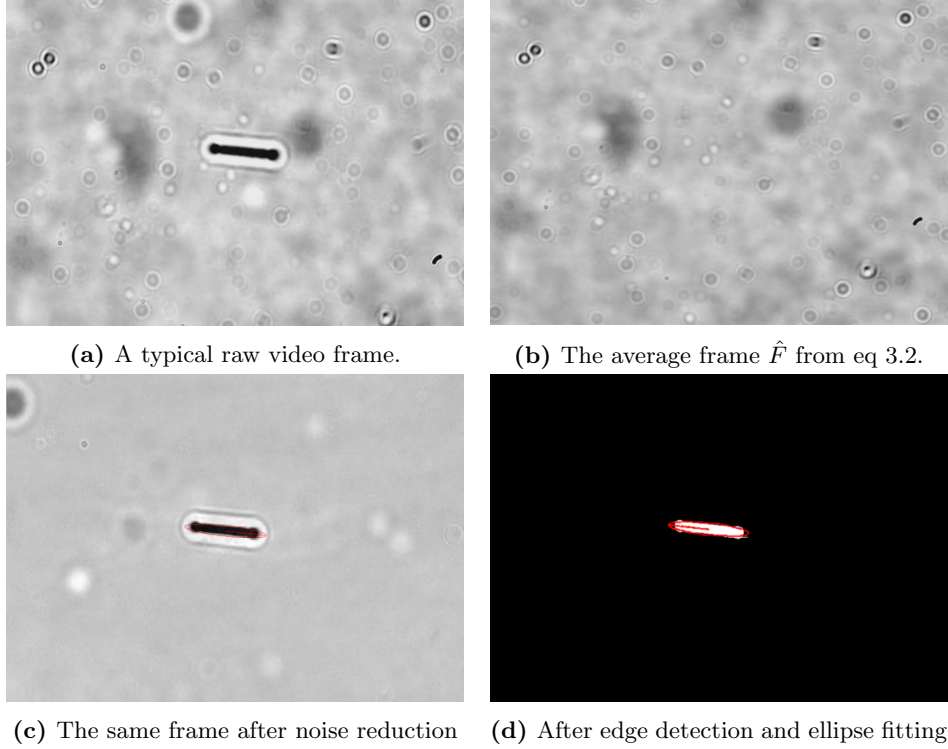


Figure 4.1: These pictures show a simplified version of the image analysis from raw image to estimated particle position

4.0.9 Estimation of orientation

The ellipsoid given by the fitting is then our best approximation of the projection of the actual particle. In order to normalize \mathbf{n} we need to know the length of the particle. It was shown by Leal [8] that the particle will always spend a majority of its time aligned with the flow, ie aligned with the camera which means that by simply calculating the length L every frame and finding the mode of the distribution we will find a good estimate of L .

So given an ellipsoid with length l_e , width d_e and angle ϕ_p we find

$$p_x = l_e \sin(\phi_p) \quad (4.1)$$

$$p_z = l_e \cos(\psi_p) \quad (4.2)$$

with x and z projection p_x and p_z . To find \mathbf{n} we normalize the projection using

$$n_x = \frac{p_x}{L}, \quad (4.3a)$$

$$n_z = \frac{p_z}{L}, \quad (4.3b)$$

$$n_y = \sqrt{1 - n_x^2 - n_z^2}. \quad (4.3c)$$

4.0.10 Width compensation

Up until this point we have assumed that the particle is a *thin* rod so that the projection \mathbf{p} onto the x and z-axes give us an accurate estimate of \mathbf{n} . However, when we are projecting a 'thick' particle with length L and width D we get \mathbf{n}' . At $\phi = 0$ this is

$$\mathbf{n}' = n'_z = n_z \cos(\theta) + D \sin(\theta) \quad (4.4)$$

which is illustrated in figure 4.2.

In order to compensate for this error we modify our projection equation 4.1 to

$$p_x = (l_e - w_e) \cdot \sin(\phi_p) \quad (4.5)$$

$$p_z = (l_e - w_e) \cdot \cos(\psi_p) \quad (4.6)$$

This will reduce the particles estimated length by w_e

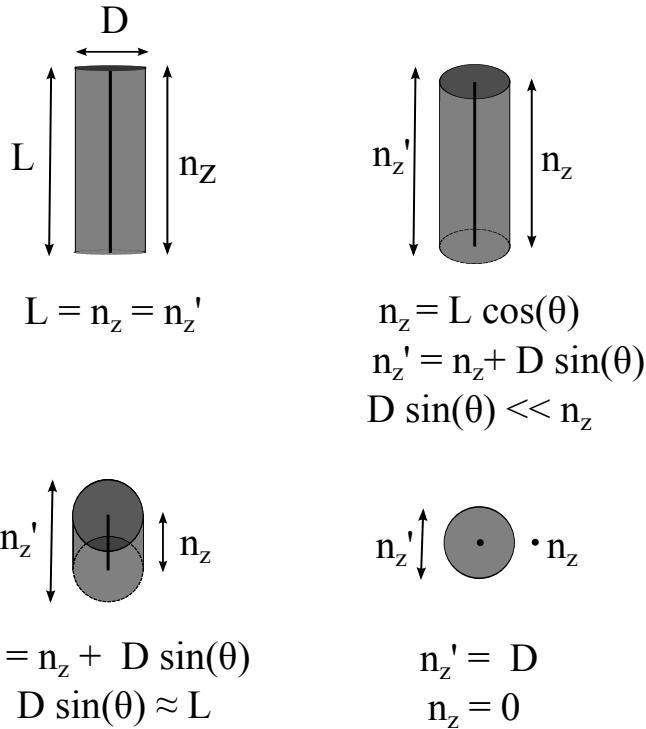


Figure 4.2

4.1 brushing

The tracking will typically have a few frames where either the particle is obstructed or is not detected correctly leading to spikes in the data. To make further theoretical analysis possible such points are removed manually. The basis for removal is simply a large discontinuity in the data, and could largely be eliminated with algorithmic means. However in particular for n_z it's very difficult to write an algorithm that will satisfactorily catch all possible edge cases. n_z have peaks that make its derivative non continuous. It's thus simpler to look at the analysis program and remove the points where the particle cannot be traced accurately due to noise.

An example of unbrushed and brushed data can be seen in figure 4.3 and all unbrushed data files will be available at [INSERTURLHERE](#)

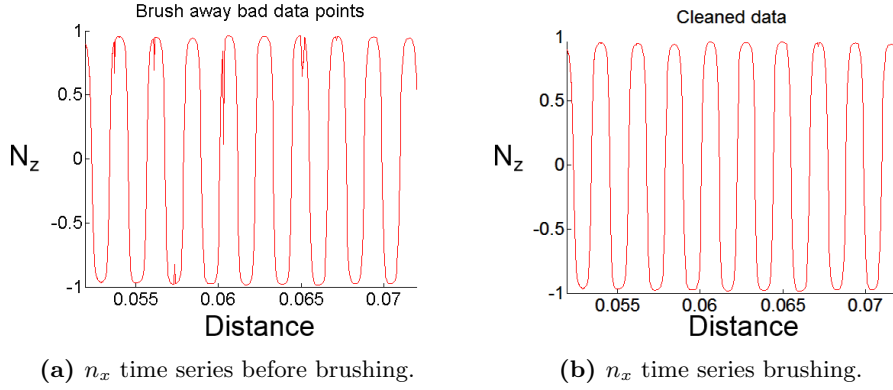
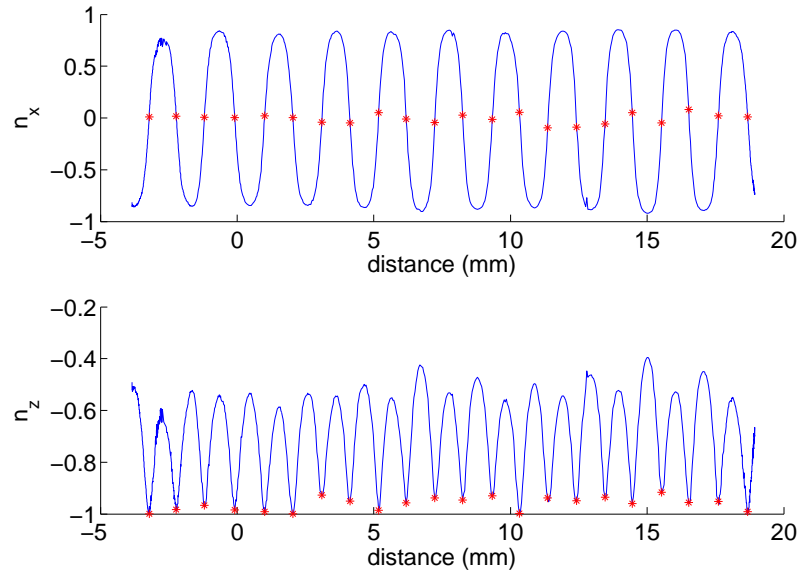


Figure 4.3: Shows a time series of n_x before and after removing points where a significant amount of noise disturbed the tracking.

4.2 Winding number estimation

As discussed in section 2.3.1, estimating the winding number for different types of orbit for one particle should allow for a rather accurate estimation of ϵ . So in order estimate the winding number for a measured particle we must identify where the θ_1 maxima and minima from figure 2.5 occur. First, the θ_2 maxima is located by where $n_x = 0$. A plot of such points can be seen in figure 4.4 where we match each n_z peak with an index i . Unfortunately data is too noisy to allow for simple algorithmic approaches to finding good local maxima. Instead we select a number of maxima $M_1, M_2 \dots M_p$ with peak index $I_1^M, I_2^M, \dots, I_p^M$ and minima m_1, m_2, \dots, m_q with peak index $I_1^m, I_2^m, \dots, I_q^m$.

We can estimate the winding number \hat{w} as the average distance between the peak indices for the maxima and minima i.e.


 Figure 4.4: The zeros of n_x and maxes of n_z

$$\overline{d_M} = \frac{1}{p-1} \sum_{j=1}^p I_{j+1}^M - I_j^M \quad (4.7)$$

$$\overline{d_m} = \frac{1}{q-1} \sum_{j=1}^q I_{j+1}^m - I_j^m \quad (4.8)$$

$$\hat{w} = \frac{\overline{d_M} + \overline{d_m}}{2}. \quad (4.9)$$

In the case that we only have 1 maxima and minima we use instead that the distance between maxima and minima should be half a period, i.e.

$$\hat{w} = |I_1^M - I_1^m| \cdot 2 \quad (4.10)$$

4.3 Matching to theoretical orbit

To find the best matching orbit from a poincare map we again utilize the n_z peaks where $\phi = 0$ which we call \mathbf{P}_z from figure 4.4. \mathbf{P}_z still is N long but now we are concerned with simply matching them with the peaks from theoretical orbits as opposed to estimating a winding number.

To find the best matching theoretical orbit we computed the least square distance for all orbits on all face maps with $\epsilon \in [0.01, 0.02, \dots, 0.1]$. If we for each orbit denote our theoretical series of n_z peaks $\mathbf{Q}_z(\theta, \epsilon)$ of length $M >> N$ we can assign a score function $S(\theta, \epsilon)$ as

$$S(\mathbf{P}, \theta, \epsilon) = |\mathbf{P}_z - \mathbf{Q}_z(\theta, \epsilon)|^2 \quad (4.11)$$

However matching against different θ and ϵ is not enough to get small mean square distance as the phase of the time series might be different. It can be assumed that P_z will be at least half a period of the quasi period θ_2 since otherwise we would have no reason to think there is quasi periodic behaviour and trying to match an orbit would be fairly pointless. If $Q_z^{(i)}$ denotes the series of peaks starting at i and P_z is at least half a period we can calculate the score for starting at a certain starting index $S(\theta, \epsilon, i)$

$$S(\mathbf{P}, \theta, \epsilon, i) = \left| \mathbf{P}_z - \mathbf{Q}_z^{(i)} \right|^2. \quad (4.12)$$

ϵ will not actually change for a single particle over r different measurements P_1, P_2, \dots, P_r , whereas θ and i (the phase) will. We find the best θ and i as

$$\hat{S}(\mathbf{P}_j, \epsilon) = \min(S(\mathbf{P}_j, \theta, \epsilon, i)) \quad (4.13)$$

and find the best ϵ using

$$\epsilon_{best} = \min\left(\sum_{j=1}^r \hat{S}(\mathbf{P}_j, \epsilon)^2\right). \quad (4.14)$$

5

Results

During the work of this thesis around 300 movies of particles have been recorded with gradual improvements to the setup in terms of density matching, particle density, bubble elimination etc. In this section we will present the data from three movies of two different particles. One referred to as particle A, the other as particle B. The measurements in this section was done together with Alexander Laas.

Each measurement was started at an approximate depth D and at position $p_0 = (x_0, z_0)$ in the channel relative to the inlet on the right, closer to the pump. Since we want the shear to be entire in the y direction we would want to be as close to $z_0 = 0$ as possible, but variations less than 1 mm should still have virtually identical shear.

In the time series plots below such as figure 5.2, the circular and star markers indicate the peaks used for estimating the winding number as explained in section 4.2. A circle is an estimated minima m_i , stars an estimated maxima M_i .

5.1 Particle A

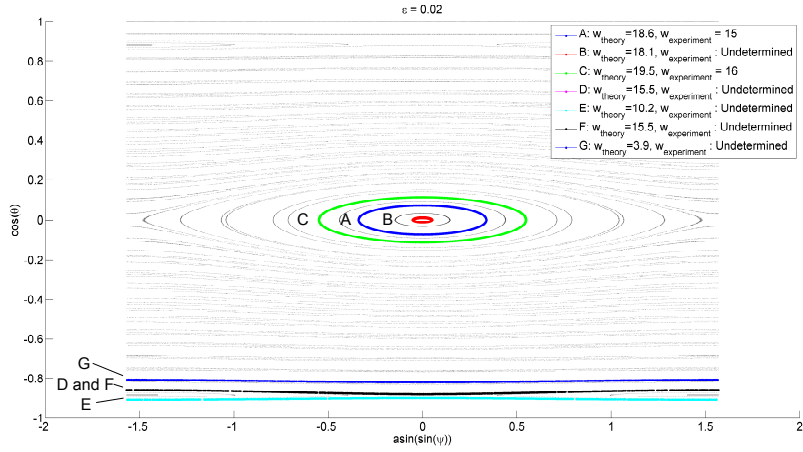


Figure 5.1: The face map for $\lambda = 8$ and $\epsilon = 0.02$. The measured λ was 8.2 ± 0.1 . The most measurements for this particle were rather constant, but the winding numbers are within 50% of the estimates but both are too low, suggesting that the ϵ might be too low.

5.1.1 Measurement 1

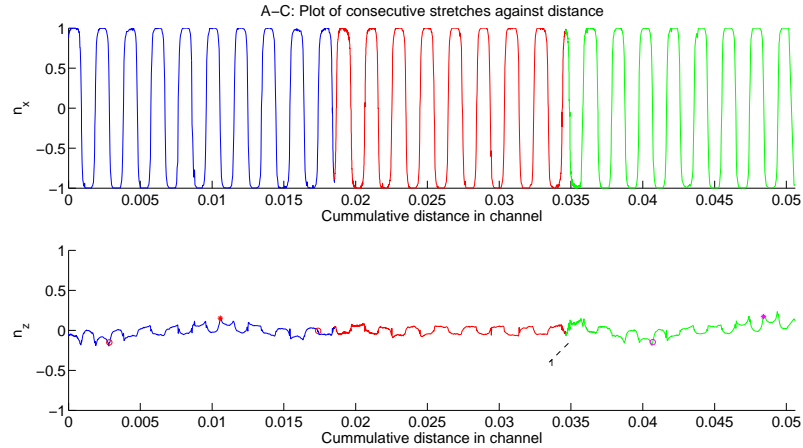


Figure 5.2: Despite being very close to a centre orbit there is very little quasi periodic behaviour. The very flattened peaks compared to a low n_z orbit in 2.3b are a result of the width compensation discussed in section 4.0.10. This particle started $x_0 = 9.8\text{mm}$, $z_0 = 8.9924\mu\text{m}$ and $D \approx 90\mu\text{m}$.

5.1. PARTICLE A

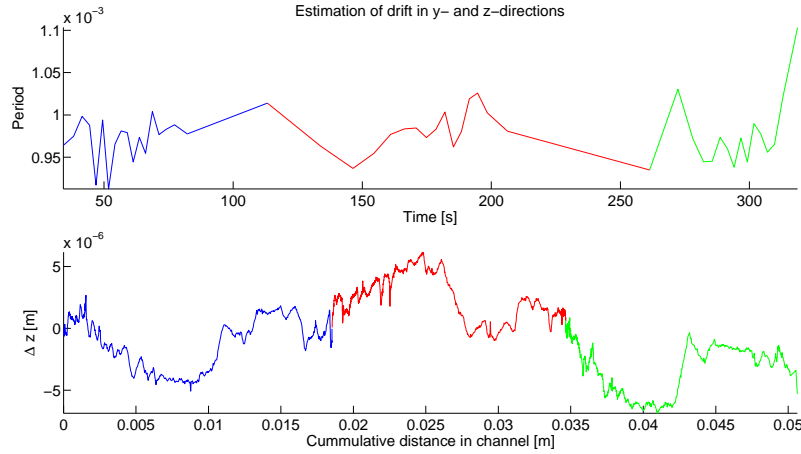


Figure 5.3: Estimating the sinking of the particle and the z position in the channel. The period here refers to the distance between two successive zeros for n_x relative to the first. There is no clear trend to higher or lower values which suggests that there is little sinking/floating. The drift in the z coordinate is also very small relative to the movements in the x direction, these are on the order of $10\mu m$ compared to the x direction which is on the order of $2 \cdot 10^4 \mu m$

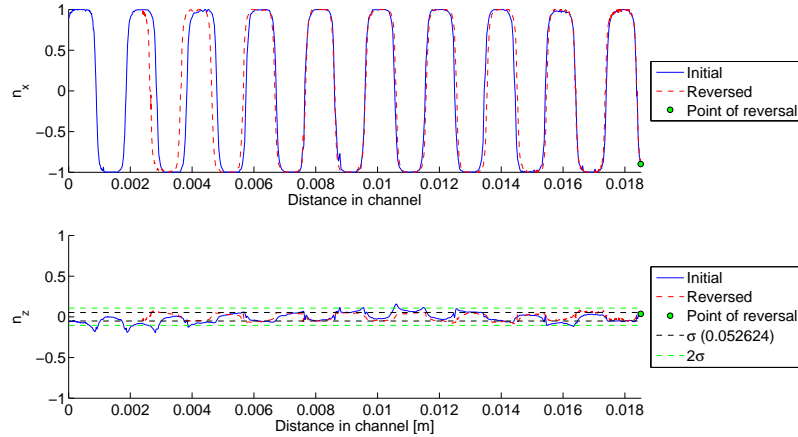


Figure 5.4: Shows n_x and n_z first and second stretches from figure 5.2 but against the actual position in the channel as opposed to commulative distance. There is an almost perfect match along the entire channel for n_x and only small disagreement for n_z . The dashed lines indicate the error margins for detecting $n_z = 0$.

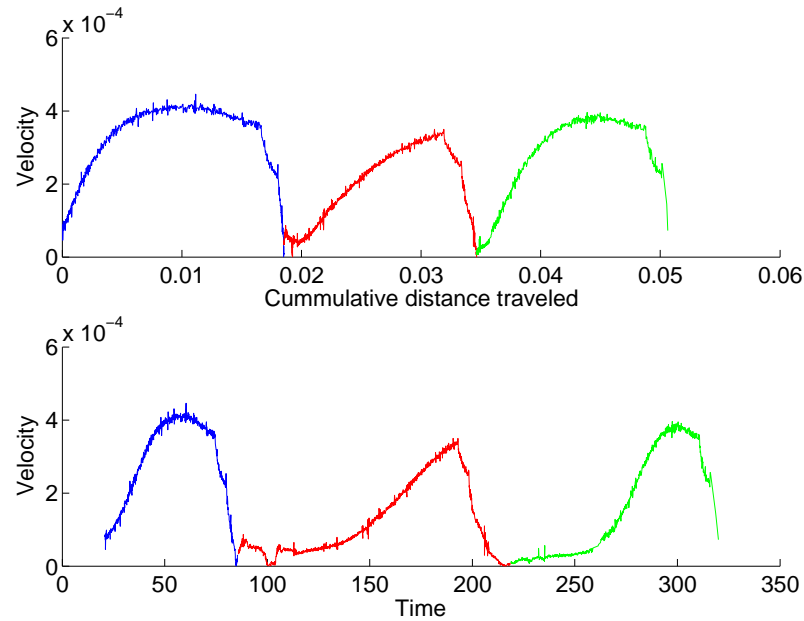


Figure 5.5: The speed (note not the velocity) of the particle against distance as well as time. The most distinct difference is in the time plot where we see in the first reversal there is a "double dip". This only and always occurs at the reversal at the far end from the pump. There is also noticeably different acceleration behaviour that is consistently different across all measurements.

5.1.2 Measurement 2

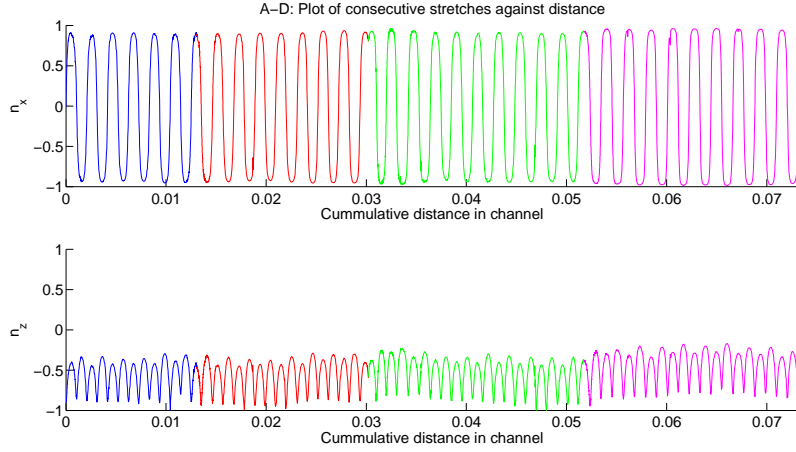


Figure 5.6: A tracked particle with a large n_z component with a very consistent periodic behaviour. $x_0 = 26.0\text{mm}$, $z_0 = 275\mu\text{m}$, $D \approx 105\mu\text{ m}$.

5.1.3 Measurement 3

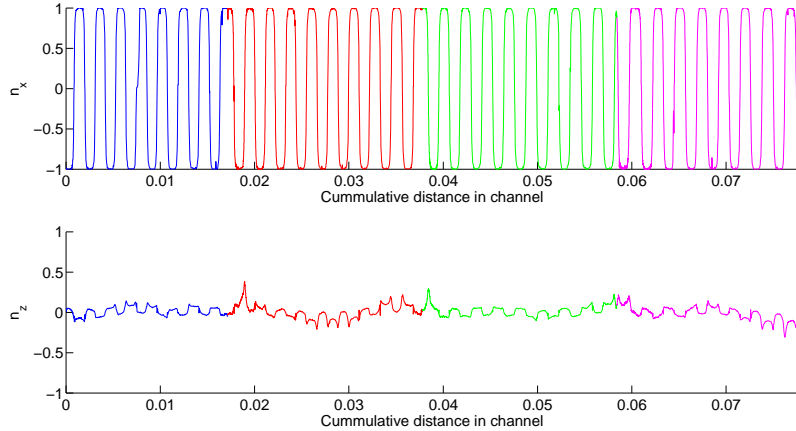


Figure 5.7: The peaks that occur after each reversal are not the cause of a tracking error but can be seen clearly in the films. The cause of such a sudden peak and then reverting back to another orbit is not known and we have no good theoretical explanation for it. We begin to break around (3) which is also where there is a change in the orbit. The particle starts at $x_0 = 12.3\text{mm}$, $z_0 = 160\mu\text{m}$, $D \approx 100\mu\text{m}$.

5.1.4 Measurement 4

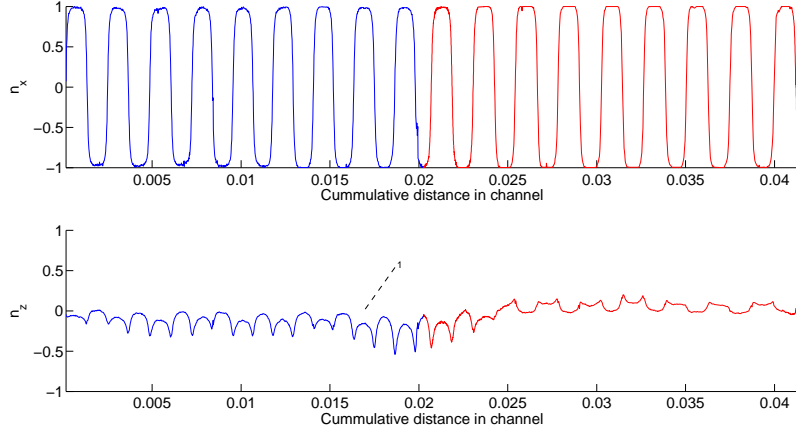


Figure 5.8: The flow is reversed when the particle is at (1) and we can see that the peaks are larger than what we would expect from the rest of the stretch. Started at $x_0 = 8.7\text{mm}$, $z_0 = 16\mu\text{m}$, $D \approx 95\mu\text{m}$.

5.1.5 Measurement 5

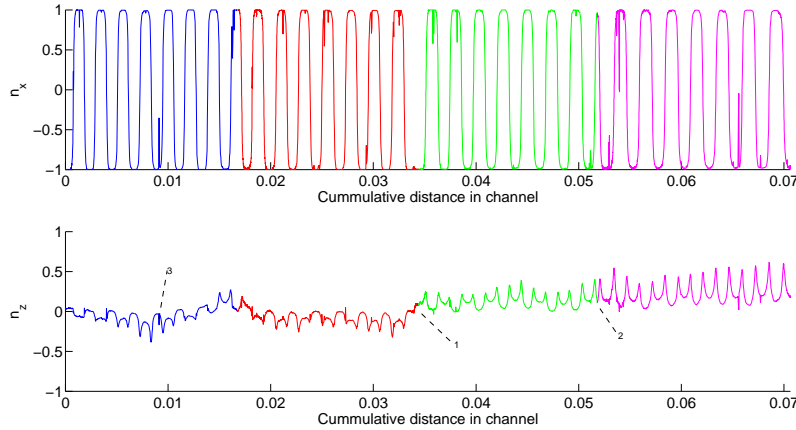


Figure 5.9: $x_0 = 10.7\text{mm}$, $z_0 = 240\mu\text{m}$, $D \approx 60\mu\text{m}$. 1: Very bad reversal. Note that this very bad reversal occurs at the "pump side" of the channel. 2: A slight change in orbit, but it is still in the same region on the SOS. 3: Data that haven't been cleaned.

5.1. PARTICLE A

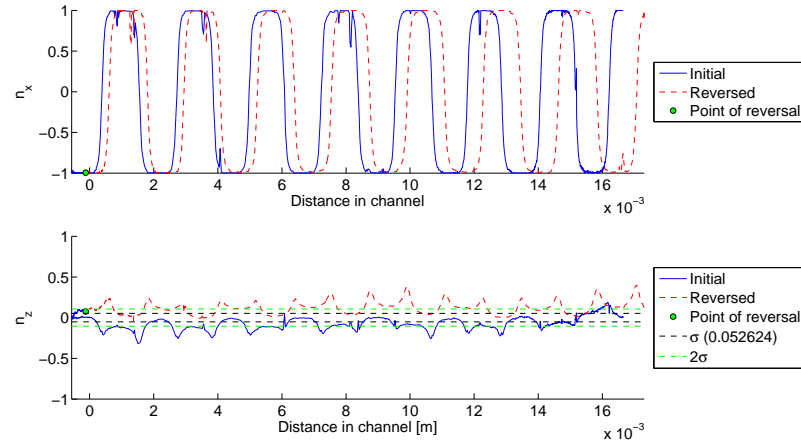


Figure 5.10: n_x and n_z from figure 5.9 for the second and third stretch plotted against actual distance instead of commutative distance. The reversal occurs at the left and although there is some moderate agreement in n_x the match in n_z is non existant from the very start.

5.2 Particle B

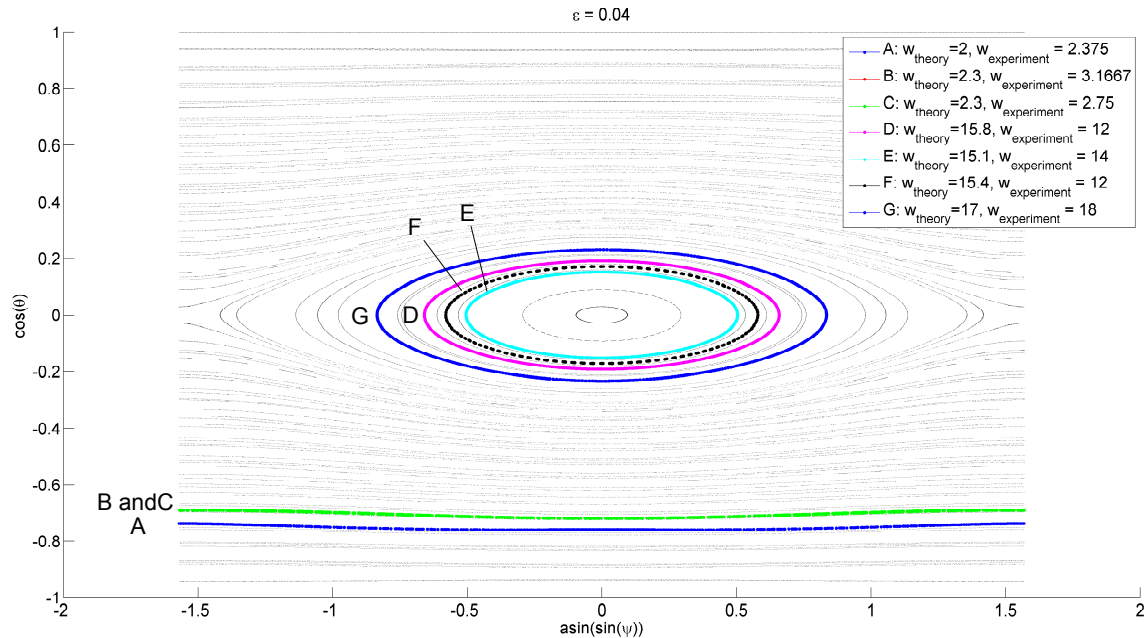


Figure 5.11: The facemap for $\lambda = 7$, the estimate of λ from measurement was 6.7 ± 0.1 .

5.2. PARTICLE B

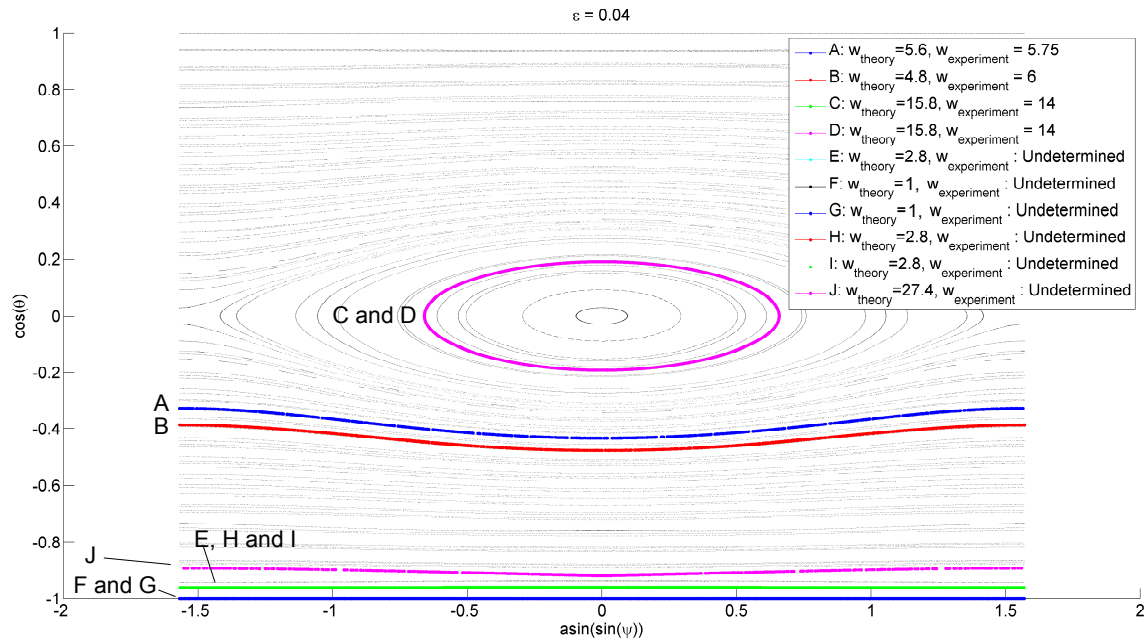


Figure 5.12: The facemap

5.2.1 Measurement 1

5.2.2 Run 1

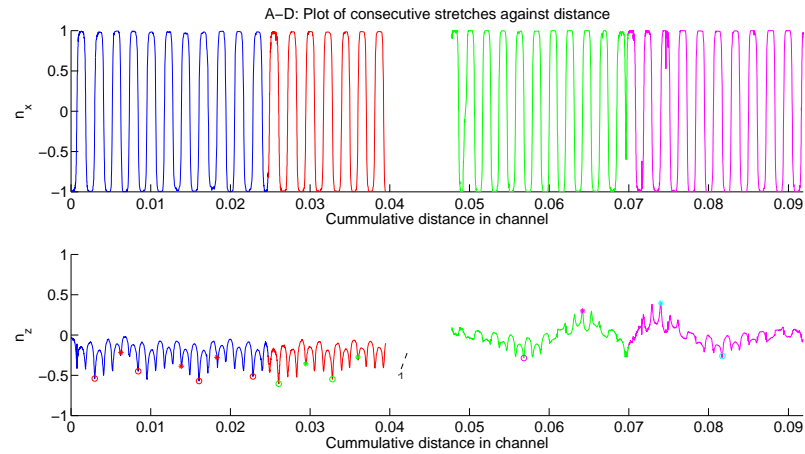


Figure 5.13: The first two stretches match very well as well as the last two. In the reversal between these two there is a large change which begins at (1) where the flow is starting to revert. This reversal also occurs at the end of the channel closer to the pump. Starts at $x_0 = 9.3\text{mm}$, $z_0 = 35\mu\text{m}$, $D \approx 100\mu\text{m}$

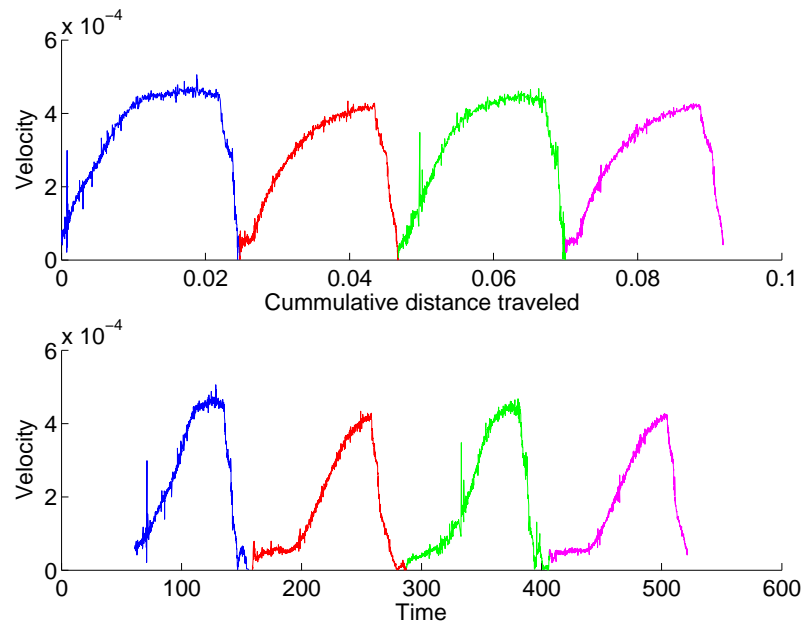


Figure 5.14: The speed of the particle against time and against position. In the plot against time there is an extra dip to 0 at around $t = 150$ and $t = 400$. This occurs only at the end of channel further away from the pump.

5.2.3 Measurement 2

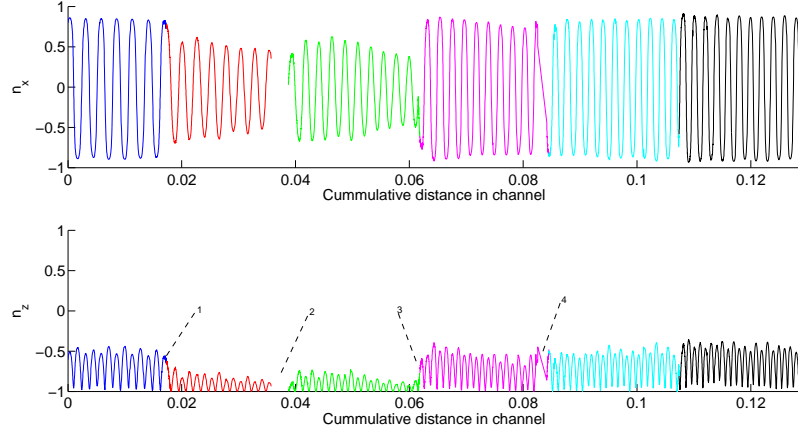


Figure 5.15: Mostly constant orbit for large n_z . The reversals at (1) and (3) both change the orbit slightly but the size of the change is exaggerated by n_z being very close to 1. The actual change in orbit can be seen in figure 5.12 is not as large as this plot might indicate. There is missing data at (2) and (4) where the particle was lost in tracking for some time. Started at $x_0 = 28.6\text{mm}$, $z_0 = 72\mu\text{m}$, $D = \approx 85\mu\text{m}$.

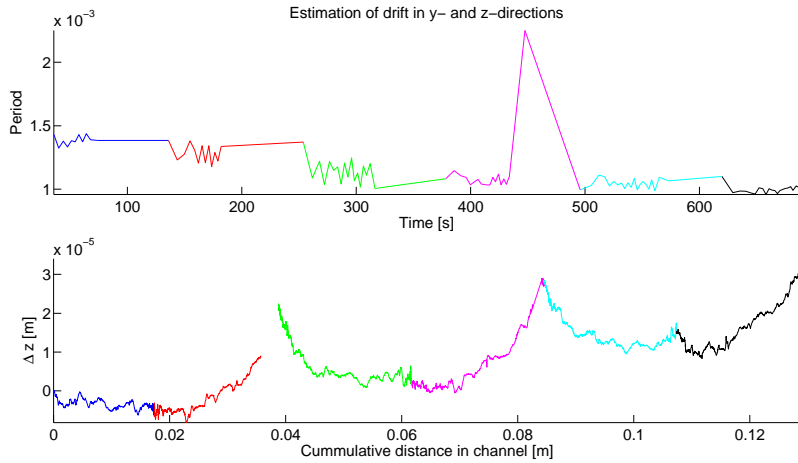


Figure 5.16: In the upper figure we see the period

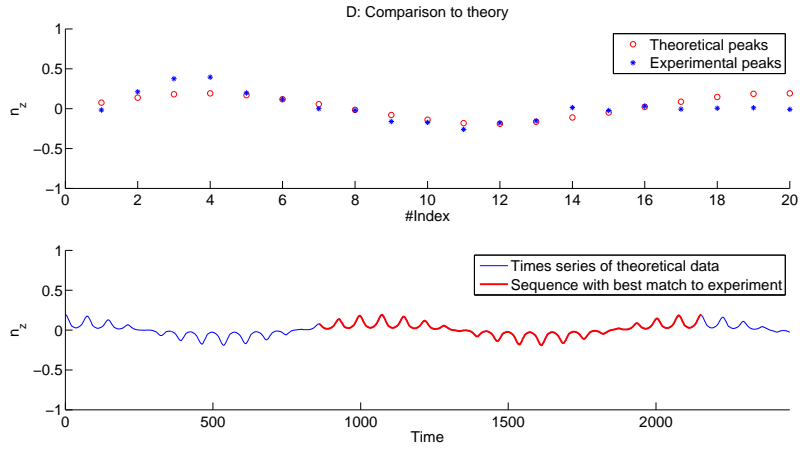


Figure 5.17: The upper figure shows the experimental n_z peaks versus the theoretical ones for the best matching orbit. The lower plot shows where what section of the theoretical time series was used for matching, ie what i from section 4.3 was chosen.

5.2.4 Measurement 3

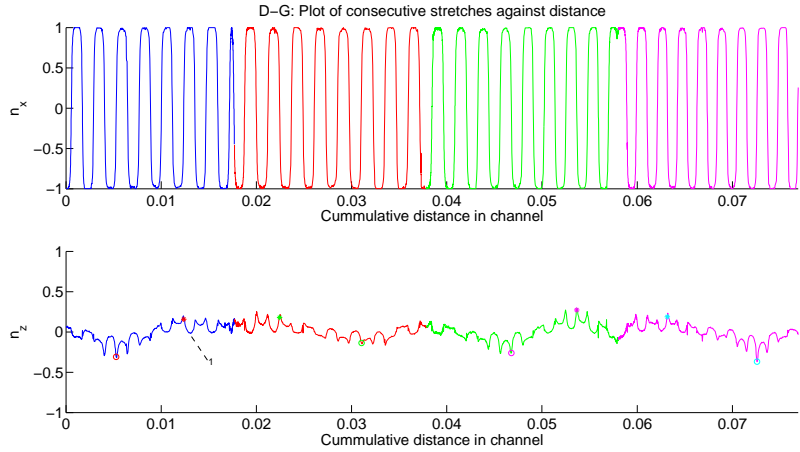


Figure 5.18: A circular quasi periodic orbit. Started at $x_0 = 2.7\text{mm}$, $z_0 = 76\mu\text{m}$, $D \approx 90\mu\text{m}$.

5.2.5 Measurement 4

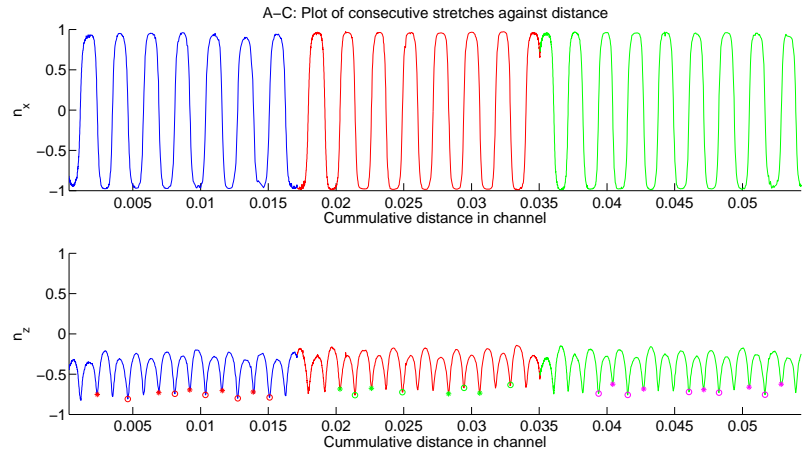


Figure 5.19: While there is not large change in n_z there seems to be some small variations that could correspond to a bent quasi periodic orbit. Started at $x_0 = 12.9\text{mm}$, $z_0 = 21\mu\text{m}$, $D \approx 85\mu\text{ m}$

6

Discussion

Looking at figures 5.11, 5.12 and 5.1 we find all three types of orbits discussed in section 2.3.1 and their winding numbers for the orbits where we can measure it also agree well with our theoretical predictions. This is however only for the stretches that do work well, and even in those measurements there are many reversals where there are large differences before and after such as in figure 5.10.

In general orbits with higher n_z have very periodic orbits, whereas low n_z do not.

We see four major problems in the data

1. Sinking
2. Bad reversals
3. Too few flips to clearly estimate winding number
4. Unexplained changes in orbit

6.1 Sinking

One of the major problems with this setup compared to the previous setup is the density matching, given a density mismatch of 0.05 g/ml we find using 2.4 a falling speed of $\frac{2}{9} \frac{0.05 \cdot 9.82 \cdot (10^{-5})^2}{2.4 \cdot 10^{-3}} =$

$4.9 \cdot 10^3 \mu\text{m}/\text{s}$. In earlier measurements the pump speed was $3 \mu\text{l}/\text{minute}$ and the particle were 60% larger, which meant the sinking occurred more than twice as long and twice as fast which meant it was a larger problem. Even now though it can be noticeably as in longer measurements such as in figures 5.15 and 5.16.

6.2 Reversals

Almost every measurement with several stretches will have on reversal where the particle noticeably changes orbit. This can been seen figures 5.9, 5.8 and 5.13. While there is a trend that bad reversals occur at he end further from the channel there are many exceptions to this. There are many cases where the orbit begins to change just as the flow is starting to reverse, such as in figure 5.8 so a possible culprit would then be that reversals occur too rapidly.

6.2.1 Velocity behaviour

A possible cause of bad reversals are too rapid reversals and to prevent this the reversals are staggered. At the start of a reversal the infusion/withdrawal rate is reduced to 50% for 10 seconds, then stopped completely for 10 seconds and reverted at 50% for another 10 seconds before resuming at full speed.

Possibly increasing this staggering on the first part might make a difference, but if we look at the plot of the speed of the particle in figure 5.5 and 5.14 we see that after a rather sharp decline in speed the acceleration is very slow. Almost all of this acceleration occurs while the pump is infusing or withdrawing at a fixed rate. Now the liquid accelerating while the pump rate constant suggests that there is a noticeably expansion in the channel. To verify this we can look more closely at he speed graphs 5.5 and 5.14.

If we have an expanded/contracted channel it should have different effects on different sides of the channel. We expect that on the side closer to the pump the expanding channel will simply absorb part of the fluid infused causing a slowed acceleration but it would start more or less right as the pump starts infusing/withdrawing. Meanwhile on the far end of the channel the 'extra' fluid

6.3. WINDING NUMBER MATCHING

in the channel could be withdrawn before any pressure is felt on the far side. This would cause a delay where there is no acceleration for some while after the pump started acceleration.

This behaviour is exactly what we see in all speed plots like 5.5 and 5.14, on reversals on the far end there is a second dip where the particle starts at $|v| = 0$ for some extra seconds. On the end closer to the pump this never occurs.

An earlier theory for the delay would be an offset in the pump, for example a distance between the syringe handle and the pump holder which would need to be traversed, but this would occur at both ends of the channel and would not explain the very long acceleration of the fluid.

6.3 Winding number matching

While using the score function \hat{S} to find the closest matching orbit is useful, it only gives the best fit and does not actually show that the orbit is close (just more close than the other ones). Instead the best tool for validating, or dismissing, a matched orbit and an estimated ϵ is the winding number for the orbits where this can be done. If we look at figure 2.6 we see that the difference in winding number of the same θ is on the order of a factor 2 between $\epsilon = 0.01$ and $\epsilon = 0.05$ for circular orbits, and still quite noticeably different between $\epsilon = 0.05$ and $\epsilon = 0.10$, especially where the change from circular to bent orbit occurs.

When we look instead at orbits for large $|n_z|$ like in figure 5.12 or for $n_z \approx \psi \approx 0$ like orbit B in figure 5.1 there is not much information to extract. The orbits for different ϵ, λ and i all largely the same, the differences are too small for us to reliably detect. This creates a problem for detecting particles with very small ϵ . For n_z that are very small, we cannot distinguish the orbits for a small ϵ particle with higher ψ orbit for a high ϵ particle with a low ψ orbit. For higher n_z we cannot distinguish straight lines from straight lines. And in the intermediary we are unable to detect a $w > 20$, at best finding a sloping n_z which might just be undesired reversals. Particle A has several orbits that are matched in the intermediary circular n_z region which we can distinguish from $\epsilon = 0$ but we can not estimate the winding number especially well as we barely have a half period. If we indeed had a circular orbit with $w = 19.5$ as predicted we need to use the end point

6.4 Unexplained behaviours

In a number of measurements there are changes in orbit for which we have no good explanation. For example in figure 5.9 the second reversal is completely sharp, the orbit virtually instantly changes, completely 'forgetting' the previous orbit. Why does this occur with the same particle, the same setup, seemingly the same conditions that produce the excellent reversals in figure 5.2. The only difference is the z coordinate, yet figure 5.7 was measured at a similar z and showed very few odd behaviours. This could be explained

7

Conclusion

The conclusion is that we found something.

A

Raw data

Bibliography

- [1] J. Einarsson, Periodic and aperiodic tumbling of microrods advected in a microchannel flow, *Acta Mechanica* (2013) 1–9.
- [2] A. Johansson, Analysis of empirical data on the tumbling of microrods in a shear flow, diploma thesis, Chalmers University of Technology (2012).
- [3] E. J., Low reynolds number particle dynamics, Master's thesis, Chalmers University of Technology.
- [4] T. Kaya, H. Koser, Characterization of hydrodynamic surface interactions of escherichia coli cell bodies in shear flow, *Phys. Rev. Lett.* 103 (2009) 138103.
- [5] A. Einstein, A new determination of molecular dimensions, *Annalen der Physik*.
- [6] G. B. Jeffery, The motion of ellipsoidal particles immersed in a viscous fluid, *Proceedings of the Royal Society A* 102.
- [7] P. J. Gierszewski, C. E. Chaffey, Rotation of an isolated triaxial ellipsoid suspended in slow viscous flow, *Canadian Journal of Physics* 56 (1) (1978) 6–11.
- [8] L. G. L. E. J. Hinch, Rotation of small non-axisymmetric particles in a simple shear flow, *J. Fluid Mech* 92 (1979) 591–608.

BIBLIOGRAPHY

- [9] I. V. R. A. L. Yarin, O. Gottlieb, Chaotic rotation of triaxial ellipsoids in simple shear flow, *J. Fluid Mech* vol 340 (1997) 83–100.
- [10] F. C. van den Bosch, lecture 1: Surfaces of section, Online material for course.
- [11] S. G. M. H. L. Goldsmith, The flow of suspensions through tubes i. single spheres, rods, and discs, *Jounrla of colloid science* (17).
- [12] D. K. O.G. Harlen, Orientational drift of a fibre suspended in a dilute polymer solution during oscillatory shear flow, *J. Non-Newtonian Fluid Mech.* 73 (1997) 81–93.
- [13] C. J. S. Petrie, The rheology of fiber suspensions, *J. of non-newtonian fluid mechanics* 87.
- [14] T. Pedley, *Introduction to Fluid Dynamics*, Department of Applied Mathematics and Theoretical Physics, University of Cambridge, Silver St., Cambridge CB3 9EW, U.K., 1997.
- [15] S. Childress, *An Introduction to Theoretical Fluid Dynamics*, Cambridge University Press, 2008, page 117 Starts the discussion of time reversibility of Stokes' Flow.
URL www.math.nyu.edu/faculty/childres/fluidsbook.pdf
- [16] G. K. Bachelor, *An Introduction to Fluid Dynamics*, Cambridge University Press, 1967, page 212 is definition of Reynolds Number, page 233 is Stokes Law.
- [17] W. E. W, Euler angles, from MathWorld—A Wolfram Web Resource. (2013).
URL <http://mathworld.wolfram.com/EulerAngles.html>
- [18] J. Munkhammar, Poincare map (2013).
URL mathworld.wolfram.com/PoincareMap.html
- [19]
- [20] A. Laas, Jeffrey orbits something, Master's thesis, Chalmers University of Technology.
- [21] Fabrication of pdms microfluidic channels (2010).
URL cismm.cs.unc.edu/wp-content/uploads/2011/03/MicrofluidicsLab.2010.pdf

BIBLIOGRAPHY

- [22] J. E. e. a. Y. N. Mishra, A microfluidic device for studies of the orientational dynamics of microrods, Proc. SPIE 8251 2825109.
- [23] Nippon Electrical Glass Co, Gap spacers for lcds: Microrods, www.neg.co.jp/epd/elm/e_prd/other/others_01.pdf.
- [24] J. Canny, A computational approach to edge detection, Pattern Analysis and Machine Intelligence, IEEE Transactions on PAMI-8 (6) (1986) 679–698.
- [25] S. N. Wijewickrema, A. P. Paplinski, C. E. Esson, Reconstruction of spheres using occluding contours from stereo images, in: Pattern Recognition, 2006. ICPR 2006. 18th International Conference on, Vol. 1, IEEE, 2006, pp. 151–154.